Freeze assisted tape casting of vertically aligned MXene films for high rate performance supercapacitors

Wenji Yang, Jae Jong Byun, Jie Yang, Francis Peter Moissinac, Yudong Peng, Gustavo Tontini, Robert A. W. Dryfe, Suelen Barg

Angaben zur Veröffentlichung / Publication details:

Yang, Wenji, Jae Jong Byun, Jie Yang, Francis Peter Moissinac, Yudong Peng, Gustavo Tontini, Robert A. W. Dryfe, and Suelen Barg. 2020. "Freeze assisted tape casting of vertically aligned MXene films for high rate performance supercapacitors." *Energy & Environmental Materials* 3 (3): 380–88. https://doi.org/10.1002/eem2.12106.

Article Category: Full Paper

Freeze-assisted Tape Casting of vertically aligned MXene films for high rate performance supercapacitors

Wenji Yang[†]*, Jae Jong Byun[δ†], Jie Yang[‡§], Francis Peter Moissinac[†], Yudong Peng[†], Gustavo Tontini[†], Robert A.W. Dryfe[‡§], Suelen Barg[†]*

†Royce Institute and Department of Materials, University of Manchester, Oxford Road, Manchester, M13 9PL, U.K.

δ Department of Electrical and Electronic Engineering, University of Manchester, Sackville Street Building, Manchester M1 3BB, U.K.

‡ National Graphene Institute, University of Manchester, Oxford Road, Manchester, M13 9PL, U.K.

§ Department of Chemistry, University of Manchester, Oxford Road, Manchester M13 9PL, U.K.

* Corresponding authors: wenji.yang@manchester.ac.uk; suelen.barg@manchester.ac.uk

Keywords: Freeze-Assisted Tape Casting; Thickness-Independent Capacitance; Vertically Aligned Electrodes; MXene; Supercapacitors

Abstract

Conventional electrode preparation techniques of supercapacitors such as tape-casting or vacuum filtration often lead to the restacking or agglomeration of two-dimensional (2D) materials. As a result, tortuous paths are created for the electrolyte ions and their adsorption onto the surfaces of the active materials can be prevented. Consequently, maintaining high rate performance whilst increasing the thickness of electrodes has been a challenge. Herein, a facile freeze-assisted tape casting (FaTC) method is reported for the scalable fabrication of flexible MXene ($Ti_3C_2T_x$) supercapacitor electrode films of up to 700 µm thickness, exhibiting homogeneous ice-template microstructure composed of vertically aligned MXene walls within lamellar pores. The efficient ion transport created by the internal morphology allows for fast electrochemical charge-discharge cycles and near thickness-independent performance at up to 3,000 mV s^{-1} for films of up to 300 µm in thickness. By increasing the scan rate from 20 to 10,000 mV s^{-1}, $Ti_3C_2T_x$ films of 150 µm in thickness sustain 50 % of its specific capacitance (222.9 F g^{-1}). When the film thickness is doubled to 300 µm, its capacitance is still retained by 60 % (at 213.3 F g^{-1}) when the scan rate is increased from 20 to 3,000 mV s^{-1}, with a capacitance retention above 97.7 % for over 14,000 cycles at 10 A g^{-1}. They also showed a remarkably high gravimetric and areal power density of 150 kW kg^{-1} at 1,000 A g^{-1} and 667 mW cm^{-2} at 4,444 mA cm^{-2}, respectively. FaTC has the potential to provide industry with a viable way to fabricate electrodes formed from 2D materials on a large scale, whilst providing promising performance for use in a wide range of applications, such as flexible electronics and wearable energy storage devices.

Introduction

Expanding the electrification of the automotive and aerospace industry, in addition to increasing the supply of renewable energy within electrical grids, calls for large-scale storage of electrochemical energy. Although batteries are the electrochemical energy storage (EES) devices commonly employed due to their high energy density, their shortcomings are that they tend to be relatively heavy and their slow charge-discharge cycles are unsuitable for certain high-performance applications [1]. Supercapacitors are alternative EES devices that could potentially overcome the limitations of batteries in some circumstances, by combining the prominent characteristics from electric double-layer capacitors which are not limited by solid-state diffusion, and pseudo-capacitors which stores energy by a faradaic process. Supercapacitors demonstrate high power densities [1], fast charge-discharge profiles, relative lightness (as opposed to batteries) and durability (ability to sustain capacitance for many cycles), which make them suited to meet the growing energy demand. However, application of these devices necessitates materials and associated fabrication methods that facilitate the creation of electrodes with high energy and power densities.

Two-dimensional (2D) materials are an ideal candidate electrode material due to their large specific surface areas [2–4]. Of recent interest are MXenes [2,3] (2D carbides and nitrides (X) of a transition metal (M)) with titanium carbide ($Ti_3C_2T_x$) being a material that falls in this classification. In addition to its high electrical conductivity [5] and aspect ratio (lateral size to thickness), $Ti_3C_2T_x$ demonstrates hydrophilicity due to the terminal functional groups (-F, -OH) anchored to the surface during the etching reaction, resulting in the ability to be spontaneously intercalated by polar organic molecules. This facilitates its processability and allows it to participate in electrochemical reactions, making it an ideal supercapacitor

electrode material [2,3,6]. Despite this, there are several challenges in the fabrication of devices that effectively utilize the properties of 2D materials.

Two common and facile methods in assembling electrodes are tape casting and vacuum filtration of a solution through a porous membrane [7,8]. These typically create a thin film electrode assembly with good flexibility and relatively strong mechanical properties [9,10]. However, the nature of these methods typically leads to a restacking of the 2D material [11] which reduces the accessible surface area and limits ion transport in thicker films. This results in electrodes whose electrochemical performance highly depends on the thickness of the film. The problem is further compounded by the in-plane alignment of 2D sheets which also lead to the formation of tortuous paths, impacting rate performance [12–14]. Limiting film thickness is a common way to avoid the accumulated stacking of 2D sheets in thicker films and induce enhanced performances in the resultant electrode [6,7,12]. However, other metrics of electrochemical performance such as areal capacitance might be hindered as a result.

Other varied strategies are employed to mitigate these limitations and facilitate ion transport. For one, the interlayer spacing between 2D sheets can be increased by intercalating with ions in a process commonly referred to as 'pillaring' [15–18]. Alternatively, introducing porosity into the 2D sheets by designing nano-architectures such as 'holes' [19–21], has also been proposed to facilitate ion transport. Nonetheless, these methods would still result in materials that have low volumetric energy storage or complex ion transport pathways that will impede the performance of the device at high charge-discharge rates [12,13].

Another fabrication method involves creating highly porous foam-like electrodes[22,23] composed of the 2D materials [22,23]. This can be seen in our previous work where a combination of lyophilisation and additive manufacturing namely, direct-ink writing (DIW)

was used to synthesize interdigitated MXene electrodes as current-collector free supercapacitors [24]. The electrodes had limited degrees of restacking and retained high porosity, which maximised surface area accessibility and ion transport. The electrodes fabricated via this method indicated promising performance with a high areal capacitance of 2.1 F cm^{-2} at 1.7 mA cm^{-2} and gravimetric capacitance of 242.5 F g^{-1} at 0.2 A g^{-1}, with a retention of 90 % for 10,000 cycles [24]. A further variety of unique assembly techniques of three-dimensional (3D) porous structures have been reported [25], seeking to increase ion mobility within the structures.

Whilst the mentioned fabrication methods demonstrate promising performance, the optimal assembly configuration for 2D materials is the vertical alignment of 2D sheets [12,26,27]. This would enable directional ion transport leading to thickness-independent electrochemical performance in thick films. This is seen in an earlier work carried out by Yu Xia et. al. [12]. The authors managed to maintain over 75 % of the capacitance (at scan rate of 2,000 mV s^{-1}) of films ranging from 40 µm to 200 µm in thickness by using a novel method of mechanically shearing a discotic lamellar liquid-crystal phase of $Ti_3C_2T_x$ with a non-ionic surfactant to enhance molecular interactions between the sheets. Although the vertical alignment of 2D materials has shown promise in sustaining high rate performance with increased electrode thickness [12,26,27], their performance is limited with losses at higher rates, especially for films that approach the industrial standard of approximately 100 µm [12].

Within this work, freeze-assisted tape casting (FaTC) is applied to overcome the stacking challenges found in fabricating 2D material electrodes, whilst maintaining vertical alignment of the 2D sheets. In addition, its ease of integration into current manufacturing supply chains, relatively low cost and scalable roll-to-roll processing makes it an appealing method for

fabricating supercapacitor electrodes formed from 2D materials with three-dimensional architecture.

FaTC is a combination of two manufacturing techniques: tape casting and ice-templating. Tape casting is a process involving a doctor blade regulating the thickness of a film formed by an aqueous colloid or slurry, on a carrier substrate, followed by some sort of drying or post-treatment processing. Korkut et. al. [10] fabricated tough, high conductive functionalized graphene films by tape casting an aqueous dispersion of functionalized graphene sheets and polymeric surfactants.

The other facet of FaTC is ice-templating. This aspect of the fabrication process is critical in ensuring the vertical alignment of the 2D sheets. By reducing the temperature of the casting bed of the film being tape-cast, a directional temperature gradient is induced. This will initiate the freezing of the tape-cast colloid. As it is more energetically favourable, ice-crystals will be formed via heterogeneous nucleation on the surface of the casting-bed and in some cases, on the surface of the material sheet. The directional growth of ice-crystals along the thermal gradient is used to template the microstructure of the film. Growth of lamellar ice-crystals exerts a force which segregates the MXene sheets at the solid-liquid interface, concentrating them between the ice crystals [28,29]. This solid-liquid phase separation is further aided by a quasi-liquid layer of oriented water molecules which decreases the surface energy of the ice and acts as a lubricating layer [30]. Ice-templating has been employed to develop high performance supercapacitor films with MXene, such as in the work demonstrated by Zhang Peng et. al. which showcases a $Ti_3C_2T_x$/CNT film with an internal porous network, exposing a greater amount of surface active sites[31,32].

FaTC is a popular manufacturing method for functionally graded structures and porous ceramics [33–38]. For example, Yu Chen et. al. [33] fabricated functionally graded acicular electrodes for solid oxide fuel cells using this method, achieving enhanced electrochemical performance. Although there has been work done on applying tape casting to nanomaterials for flexible electronics and EES devices [37–40], the effectiveness of this method to produce electrodes with thickness independent performance and its application to other functional 2D materials beyond graphene, is still to be realised. Yoon Hwa et. al. [41] successfully applied the FaTC method in creating aligned graphene-oxide-sulphur cathodes, to mitigate sulphur reconstruction and facilitate lithium ion transport in lithium-sulphur batteries.

In this work, we demonstrate the feasibility of FaTC for the scalable manufacturing of electrodes composed of vertically aligned 2D MXene microstructures. Based on the single or few layer $Ti_3C_2T_x$ preparation and exfoliation method developed in our previous work [24], we formulated viscoelastic $Ti_3C_2T_x$ aqueous slurries suitable for FaTC without the addition of binders or conductive agents. By adjusting ice-templating parameters within the freeze-tape casting bed, vertically aligned $Ti_3C_2T_x$ films with thickness of 150, 200, 300, 400, 500 and 700 µm were obtained and evaluated with electrochemical performance testing. Supercapacitors constructed with electrodes with thicknesses between 150 and 300 µm exhibited near thickness-independent electrochemical performance for current densities of up to 100 A g^{-1} and scan rates of up to 3000 mV s^{-1}. As a consequence of the meticulous quality control steps during the $Ti_3C_2T_x$ exfoliation and the vertical aligned microstructural design of the films, these electrodes showed a gravimetric and areal energy density of 2.8 Wh Kg^{-1} and 1.8 µWh cm^{-2} for 150 µm films; and 2.6 Wh Kg^{-1} and 11.3 µWh cm^{-2} for 700 µm films. They further achieved a gravimetric power density of 150 kW kg^{-1} at 1,000 A g^{-1} and an areal power density of 667 mW cm^{-2} at 4,444 mA cm^{-2} (700 µm). The vertically aligned $Ti_3C_2T_x$ films further retain good

flexibility and mechanical properties demonstrating their potential in a broad range of application areas, such as flexible electronics and wearable energy storage devices.

Results and discussion

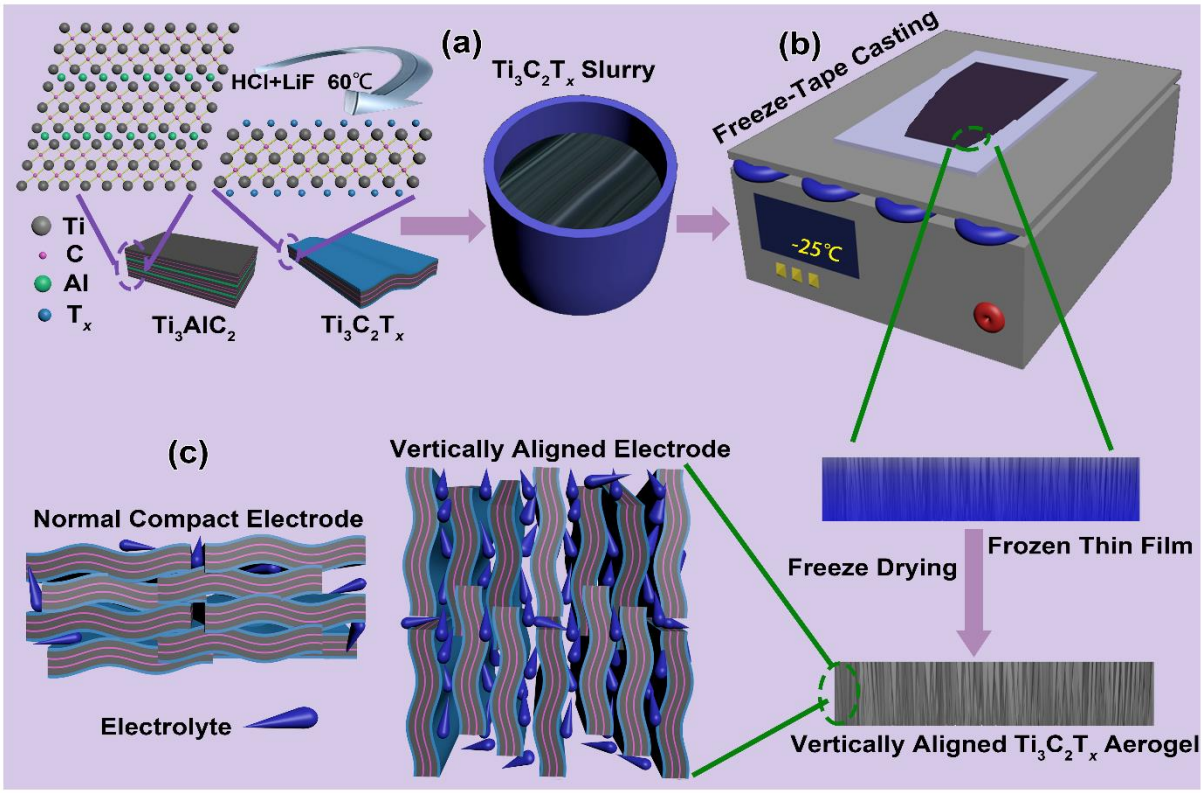

Figure 1. **Schematic representation of the manufacturing process of vertically aligned $Ti_3C_2T_x$ films through unidirectional freezing assisted tape casting (FaTC). a) MILD (Minimal Intensity Layer Delamination) synthesis of few layers $Ti_3C_2T_x$ at 60 ℃ and their formulation into castable slurries; b) FaTC of MXene slurries into vertically aligned aerogel films; c) representation of electrolyte impregnation and path within the aligned electrodes developed in this work in comparison with traditional compact morphologies.**

The manufacturing strategy of the 3D porous $Ti_3C_2T_x$ aerogel films with the vertically aligned microstructure is illustrated in **Fig. 1**. Firstly, the MILD method [42,43] (etching with hydrochloride and lithium fluoride) was chosen to etch the precursor Ti_3AlC_2 (flakes < 10 µm) to the delaminated single or few layered $Ti_3C_2T_x$ at 60 °C (**Fig. 1a**). After the concentrated

single or few layered $Ti_3C_2T_x$ aqueous paste were produced, slurries with specific concentrations (45, 70 and 120 mg mL^{-1}) were prepared for the subsequent casting (**Fig. 1b**). During FaTC, the $Ti_3C_2T_x$ slurry was deposited on the upper surface of a pre-cooled aluminium plate (at –25 °C) using a doctor blade to spread the slurry with a fixed thickness, and the film was frozen onto the substrate. The frozen $Ti_3C_2T_x$ films were subsequently freeze-dried to obtain the vertically aligned $Ti_3C_2T_x$ aerogels. A schematic comparison between stacked electrodes typically made by conventional methods and a vertically aligned porous electrode as made by our method (**Fig. 1c**) represents the improved accessibility of the electrolyte in the latter allowing for a larger surface of active material to be reached by ions, improving the efficiency of electrochemical mechanisms.

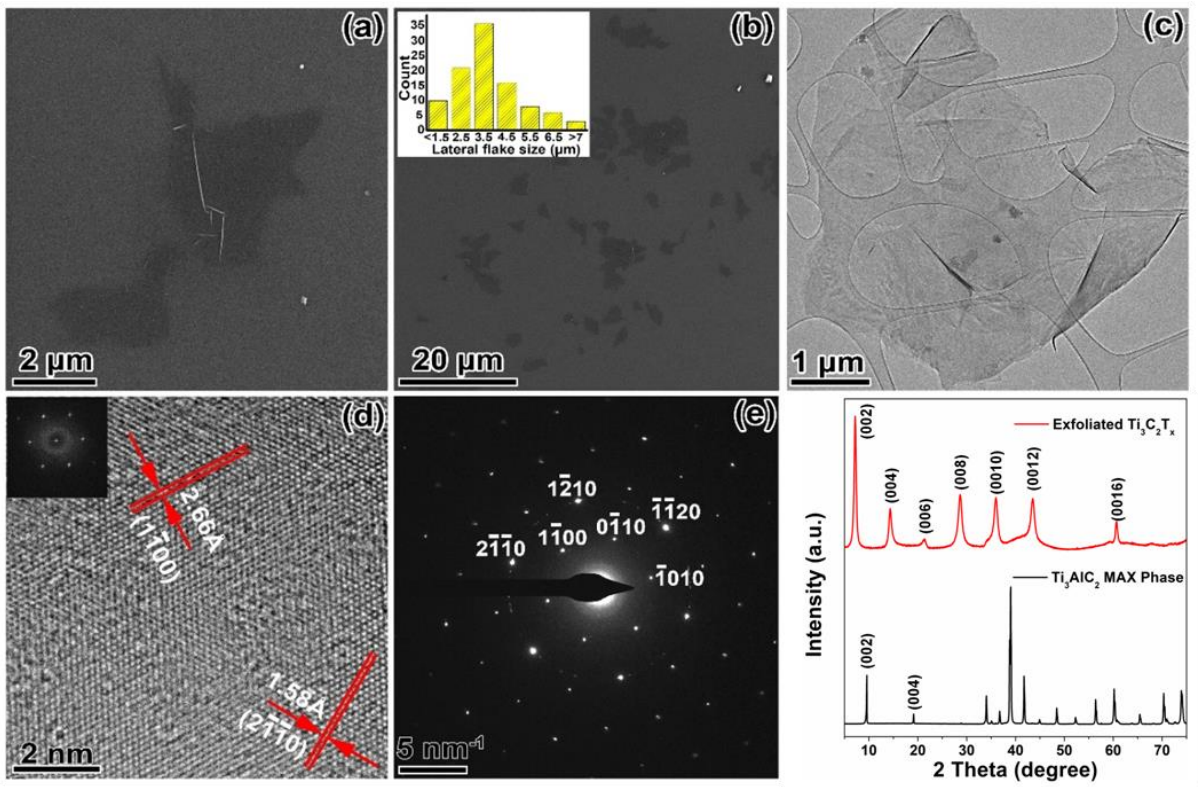

Figure 2. **Characterization of exfoliated $Ti_3C_2T_x$ flakes. (a-b) SEM images of $Ti_3C_2T_x$ flakes prepared by drop casting from a dilute $Ti_3C_2T_x$ solution in water on silica plates. The inset in (b) shows the lateral size distribution of $Ti_3C_2T_x$ flakes, measured from SEM images of over 100 flakes. (c) Low-**

magnification TEM image, (d) HRTEM (high-resolution TEM) and (e) SAED patterns of the delaminated $Ti_3C_2T_x$ flakes. (f) XRD patterns of the exfoliated $Ti_3C_2T_x$ and precursor Ti_3AlC_2.

The typical morphology of the $Ti_3C_2T_x$ flakes obtained by the etching process is shown in **Fig. 2a-b**. An average lateral flake size of 3.7 µm is obtained from the size distribution measured from scanning electron microscopy (SEM) (inset of **Fig. 2b**). The low-magnification TEM image reveals a quite thin and transparent flake on the lacey carbon grid (**Fig. 2c**). The HRTEM image in **Fig. 2d** shows the single crystallinity of the $Ti_3C_2T_x$ flake basal plane, and the measured interplanar spacings in the figure are 2.66 Å and 1.58 Å corresponding to the $(0\bar{1}10)$ and $(2\bar{1}\bar{1}0)$ lattice planes, respectively. The selective area electron diffraction (SAED) pattern (**Fig. 2e**) shows that the $Ti_3C_2T_x$ flakes in this area maintain crystallinity and the hexagonal symmetry of the basal planes of the precursor Ti_3AlC_2 MAX phase. The XRD patterns of the exfoliated $Ti_3C_2T_x$ and precursor Ti_3AlC_2 and are shown in **Fig. 2f**. The $Ti_3C_2T_x$ sediment is separated from the exfoliated $Ti_3C_2T_x$ during exfoliation and post etching washing process. In terms of the diffraction pattern for exfoliated $Ti_3C_2T_x$, all identified peaks can be attributed to the basal planes of $Ti_3C_2T_x$ as assigned and in accordance to the literature for MILD synthesis [44]. The large d-spacing of ~ 12.3 Å observed for the (002) plane at 7.19 degrees and the absence of non-basal reflections indicate the successful exfoliation of the flakes. Meanwhile, although also exhibiting the (002) peak of the exfoliated $Ti_3C_2T_x$ phase, the XRD pattern of the sediment (**Fig. S1**) also indicates the presence of the precursors Ti_3AlC_2 (PDF 04-012-0632 [45]) and LiF (PDF 00-004-0857 [46]), by-product α-Al_2O_3 (PDF 04-004-2852 [47]), and $TiC_{0.62}$ (PDF 04-017-1603 [48]). Since this mixed product influences negatively both the control of the FaTC process and the electrochemical properties of the material, it is crucial to highlight the importance of a thorough washing process.

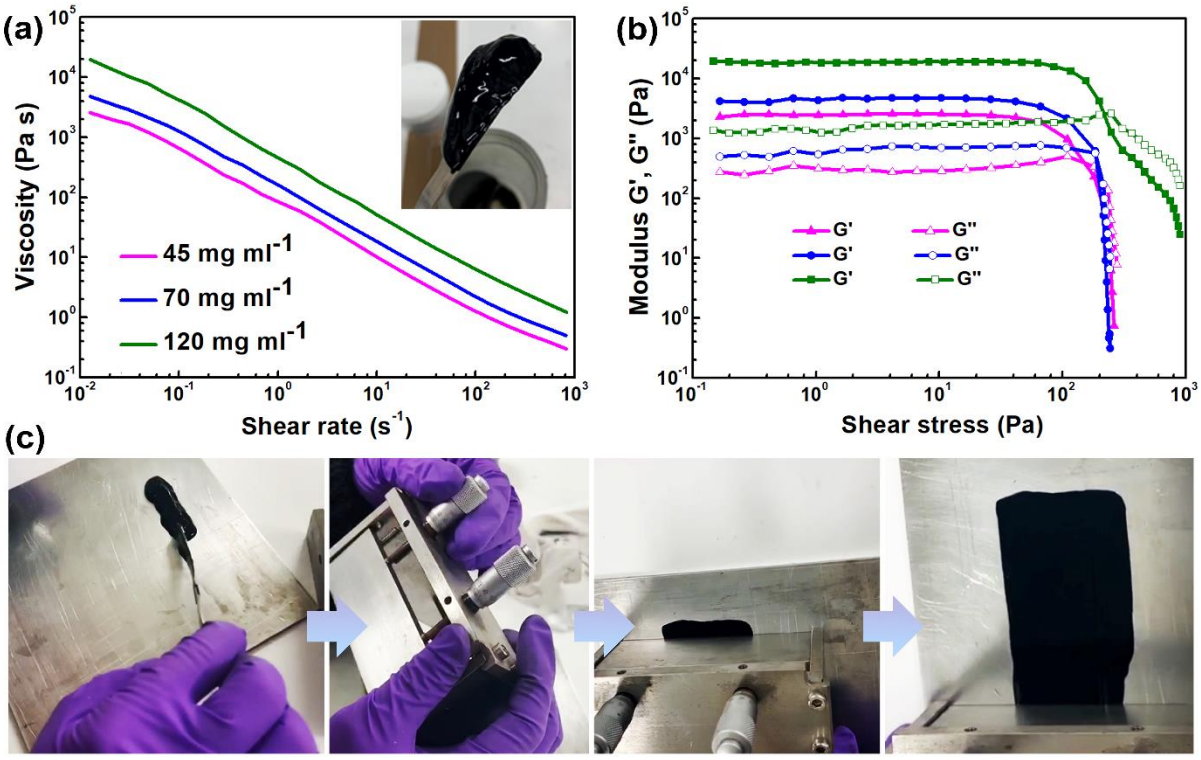

Figure 3. **(a-b) Rheological properties of $Ti_3C_2T_x$ slurries prepared with 45, 70 and 120 mg mL^{-1} flakes concentration. (a) Viscosity *versus* shear rate (inset optical camera image depicts the viscous feature of 45 mg mL^{-1} ink), (b) Viscoelastic properties (storage and loss modulus as a function of shear stress. (c) Optical camera images of the processing of a $Ti_3C_2T_x$ slurry into a film via FaTC. From left to right: slurry cast onto the aluminium plate; doctor blade adjusted to produce the desired film thickness; slurry spread onto the aluminium plate at –25 °C to fabricate film with vertically aligned MXene porous structure.**

Rheological properties such as viscosity and viscoelastic properties are key to enable the fabrication of homogeneous films of controllable thicknesses via FaTC method. Therefore, rheological investigations were carried out to identify the processability of the water based $Ti_3C_2T_x$ slurries at concentrations of 45, 70 and 120 mg mL^{-1} (**Fig. 3**). According to the viscosity versus shear rate curves in **Fig. 3a**, all slurries of varying concentrations show distinct shear thinning behaviour. The shear thinning behaviour of the slurries ensures that the MXene flakes are spread evenly during the tape casting process [42]. In order to define the linear and non-linear viscoelastic properties of these slurries, the variation tendency of both the storage

modulus (G') and the loss modulus (G") were investigated regarding the applied shear stress in the range 0.1 to 1,000 Pa at a constant angular frequency of 10 rad s^{-1} (**Fig. 3b**). Until a critical oscillation stress (above 100 Pa), both moduli stay level with G' presenting higher values than G''. Since the small shear stress oscillation demanded minor structure deformation, the slurries behave in a more elastic than viscous manner and show a linear viscoelastic behaviour. After the crossover point (150.5, 186.1 and 216.7 Pa for 45, 70 and 120 mg mL^{-1} slurries respectively), all three slurries exhibited non-linear viscoelasticity where the storage moduli dropped rapidly due to the breakdown of the weak force acting between the single/few-layer $Ti_3C_2T_x$ flakes as a result of the applied shear stress [49]. A sufficient storage modulus allows the films to retain their thickness, even after removal of the applied shear force [50]. The storage modulus in the linear elastic region increases with increased concentration of the MXene flakes (reaching 18, 991 Pa for 120 mg mL^{-1}). However, even with the lowest concentration of 45 mg mL^{-1}, the storage modulus is high enough to allow the slurries to retain its shape after casting.

The developed $Ti_3C_2T_x$ slurries have shown favourable rheological properties to produce homogeneous films of adjustable thickness between 150-700 µm, while simultaneously enabling the formation of lamella ice crystals that template pores between vertically orientated MXene interconnected flakes (**Figs. 3c**, **4 and S2**). However, the highest concentration of $Ti_3C_2T_x$ investigated in this work, induced swifter freezing of the slurries, due to the lower water content. Therefore, thinner films were more difficult to produce with the highest concentrations (120 mg mL^{-1}). This could be overcome by controlling the casting speed (the speed at which the doctor blade was applied to slurries) by the development of an automated casting system.

Typically, tape-casting process requires a relatively high-loading of colloids [49], but this could have adverse effects on ice-templating. During freezing of concentrated colloids at low growth velocities, the fraction of 2D sheets at the interface increases, which may lead to increased loading of the sheets at the freeze front. This may induce ice-crystal growth perpendicular to the thermal gradient in a phenomenon called ice-lensing [51,52]. Consequently, the resultant material would have alternating layers of ice and re-stacked 2D sheets. These cumulative factors need to be carefully considered when developing the fabrication method to manufacture vertically aligned MXene sheets via FaTC.

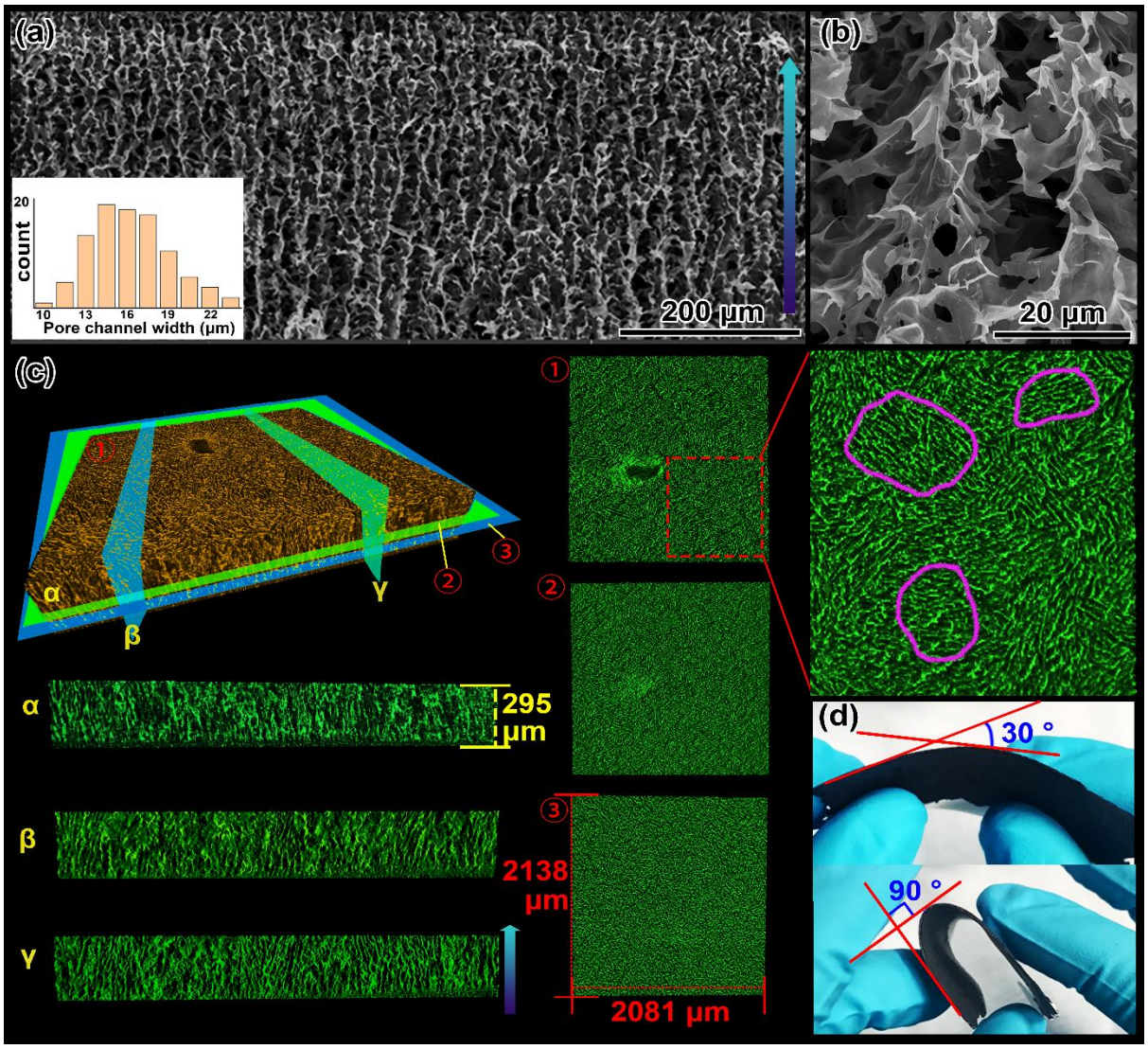

Figure 4. **Microstructural and flexibility investigation of vertical aligned $Ti_3C_2T_x$ films produced from FaTC of 70 mg mL^{-1} slurry. (a, b) SEM cross-sectional images of the film's internal microstructure. The inset in (a) depicts the pore width distribution. (c) X-ray CT images of the $Ti_3C_2T_x$ film showing: The 3D reconstruction of a volume of interest within the sample; Views onto ①-③ (corresponding approximately to the view perpendicular to the freezing direction) demonstrate the alignment of the pores and the domains organization (purple rings) within the structure; Views onto α-γ (corresponding to the view parallel to the freezing direction) show the lamellae architecture with the alignment of the $Ti_3C_2T_x$ sheets within the region. The arrow in SEM and CT images represent the freezing direction. (d) Digital photographs of a $Ti_3C_2T_x$ film with a thickness of 300 µm, showing its flexibility during bending.**

The control of the solids loading in the slurry provides direct control of the density of freeze-dried films, and so represent an opportunity to control their physical and electrochemical properties via the FaTC approach. Slurries of 45 and 70 mg mL^{-1} resulted in films of average 43.1 and 71.7 mg cm^{-3} density, respectively. The morphology of typical films produced from 70 mg mL^{-1} is shown in **Fig. 4.** The cross-sectional SEM image (parallel to the freezing direction) of a ~ 400 µm thick sample (observing a decrease in the final thickness of the film after freeze drying; final thicknesses are listed in **Table.S1**) reveals the three-dimensionally uniform porous lamellar microstructure composed of vertically aligned $Ti_3C_2T_x$ flakes (**Figs. 4a** and **4b**). The lamellae channels are 16.2 µm wide on average as measured from the SEM micrographs (the size distribution is depicted in the inset of **Fig. 4a**). These channel between $Ti_3C_2T_x$ vertically aligned walls offer significant advantages for the absorptions of the electrolyte and transportation of the ions, especially for the furthest part to the opposite electrode.

The interconnected-lamellar/cellular structures observed in **Figs. 4a** and **4b** are a result of the growth of lamellar ice-crystals and segregation of the MXene sheets within it, which is dependent on the freeze-front (interface of growing ice-crystals and colloid) velocity[53]. This is governed by the cooling rate of the casting bed (aluminium plate) i.e. the induced thermal

gradient. At low growth velocities, the freeze-front is planar [53,54], and as such the 2D sheets would be pushed to the top surface of the tape-casted film. However, this planar interface can be destabilized by Mullins-Sekerka instabilities, which are a sinusoidal perturbation arising from the interface at the solidification front [55]. They are the result of isotherms being compressed in front of a protrusion with the consequent latent heat produced diffusing more readily in this area. This results in faster growth of the protrusion to a certain direction [55] (stabilized by surface tension), resulting in the desired directional lamellar ice morphology. At rapid interface velocities, the freeze-front will become planar again, as the 2D sheets will be engulfed by the ice crystals preventing redistribution or ice-templating effects [53,54]. Ascertaining from the obtained morphology of the films (**Figs. 4a, 4b and S2**) from the FaTC process, and given an average MXene flake size of 3.7 µm, we can infer an intermediate freeze front velocity that is between unstable and metastable regimes [54]. To further analyse the morphology and 3D homogeneity of a ~ 300 µm thick $Ti_3C_2T_x$ film, X-ray CT was performed (**Fig. 4c**)**.** The analysis enabled the reconstruction of a large sample volume of ~ 300 µm thickness (the actual film thickness) and ~ 2 mm sides. Although X-ray CT's resolution cannot define the MXene sheets as well as the SEM micrographs, cross-sectional views parallel to the freezing direction (views onto α-γ) show similar vertical lamellae alignment throughout the investigated 2 mm volume of the film. Furthermore, tomography top views perpendicular to the freezing direction (Views onto ①-③) show the formation of incoherently aligned orientation domains (examples of domains are identified with the purple boundaries drawn in the enlarged view onto ①). This is predominantly caused by the heterogeneous nucleation of the ice-crystals on the substrate and their anisotropic growth behaviour further imposing constraints to the nucleation and growth of adjacent crystals, generating clusters with short-

range orientation [28,56]. Bai et al. proposed a dual temperature gradient method to control these domains achieving both vertical and horizontal alignment [57].

The developed films are flexible and mechanically robust, which plays an advantage in order to maximize the utilization of the $Ti_3C_2T_x$ electrode films in wide areas, like for the fabrication of wearable supercapacitors. As exemplified in **Fig. 4d**, a 300 µm thick $Ti_3C_2T_x$ film can be bent at an angle of nearly 180 degrees, remaining macroscopically undamaged, demonstrating its robustness for potential application in flexible and wearable devices.

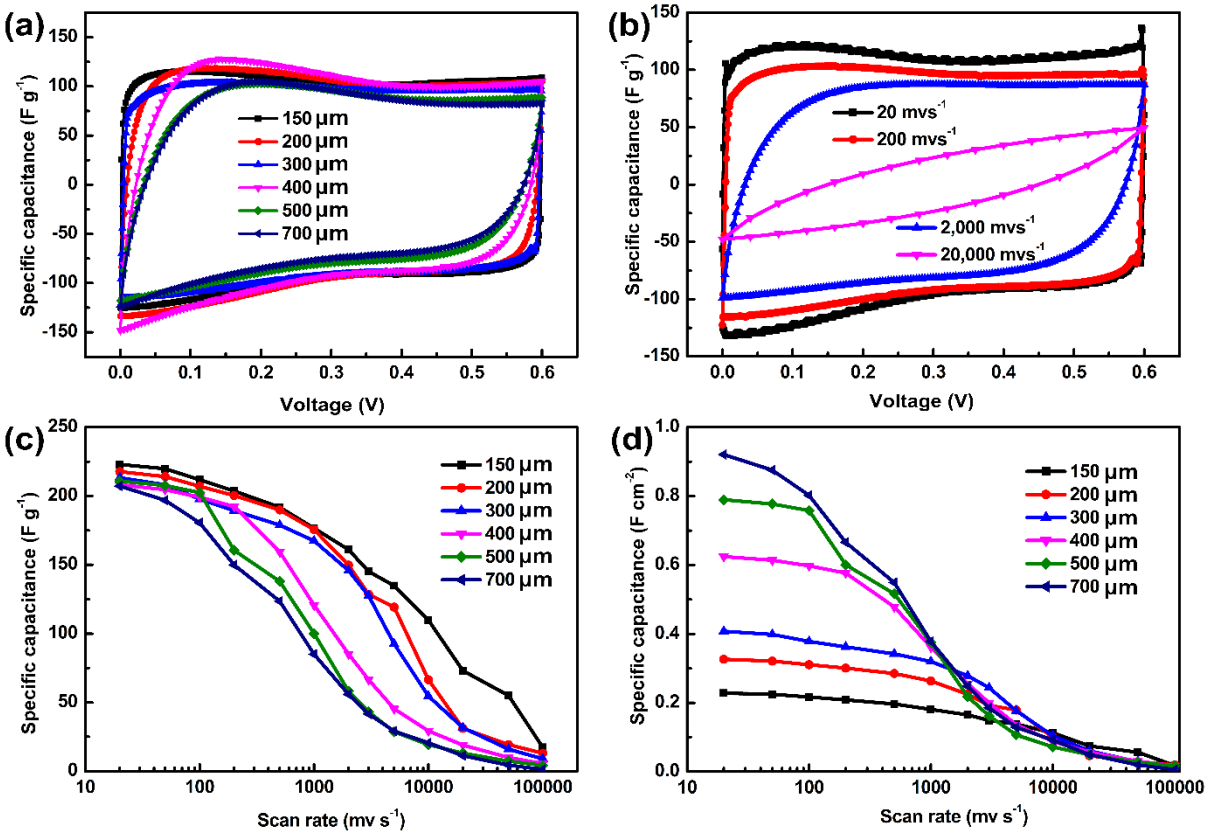

Figure 5. **Electrochemical analysis of the vertically aligned $Ti_3C_2T_x$ films with thickness of 150, 200, 300, 400, 500 and 700 µm (produced from 70 mg mL^{-1} slurry). (a) Cyclic voltammograms (CV) of the samples at the scan rate of 200 mV s^{-1}. (b) CV of the 300 µm thick $Ti_3C_2T_x$ film at scan rates of 20, 200, 2,000 and 20,000 mV s^{-1}. (c, d) Rate performance (including gravimetric and areal) of the films at scan rates ranging from 20 to 100,000 mV s^{-1}.**

To investigate the effectiveness of our approach for high rate performance applications, we have prepared two-electrode supercapacitor devices based on vertically aligned $Ti_3C_2T_x$ films produced from 70 mg mL^{-1} slurries with thickness of 150, 200, 300, 400, 500 and 700 µm. The cyclic voltammograms of the corresponding two-electrode supercapacitors based on films with varying thicknesses at a scan rate of 200 mV s^{-1} with a 3 M H_2SO_4 solution as the electrolyte are depicted in **Fig. 5a**. Almost all the CVs have maintained the typical rectangular shape, and the curves almost overlap when the thickness of the electrode varies from 150 to 400 µm. When the electrode thickness was increased to 500 and 700 µm, a slight shrinkage in the CV shape is observed due to the rising resistance. The electrochemical behaviour of the ordered vertically aligned porous structure shows an efficient mass transfer of the electrolyte ions despite the increase in the thickness of the electrode. Considering that the conventional electrode thickness is usually less than 100 µm [58–60], the modified structure created by the FaTC method shows a great advantage in increasing the electrode thickness without sacrificing the electrochemical performance. **Fig. 5b** shows the CVs of a 300 µm thick sample at a large range of representative scan rates from 20 to 20,000 mV s^{-1}. When the scan rate was gradually increased from 20 to 3,000 mV s^{-1}, the rectangular shapes of the CV curves are retained, indicating the high rate performance of $Ti_3C_2T_x$ with this vertical porous structure (**Figs. 5b** and **S3**). The gravimetric and areal capacitance of samples with various thicknesses at different scan rates are shown in **Figs. 5c** and **5d**, respectively. With the enhancement of the scan rate value, the corresponding specific gravimetric capacitance of all thickness show very modest distortion, especially below 100 mV s^{-1}. For film thicknesses up to 300 µm, and scan rates up to 3,000 mV s^{-1}, the electrodes are still able to yield a comparatively high specific capacitance (127.4 F g^{-1}). The areal rate performance of the films shows that for thicknesses

of up to 300 µm the capacitance is well maintained when the scan rate is increased up to 3,000 mV s^{-1}.

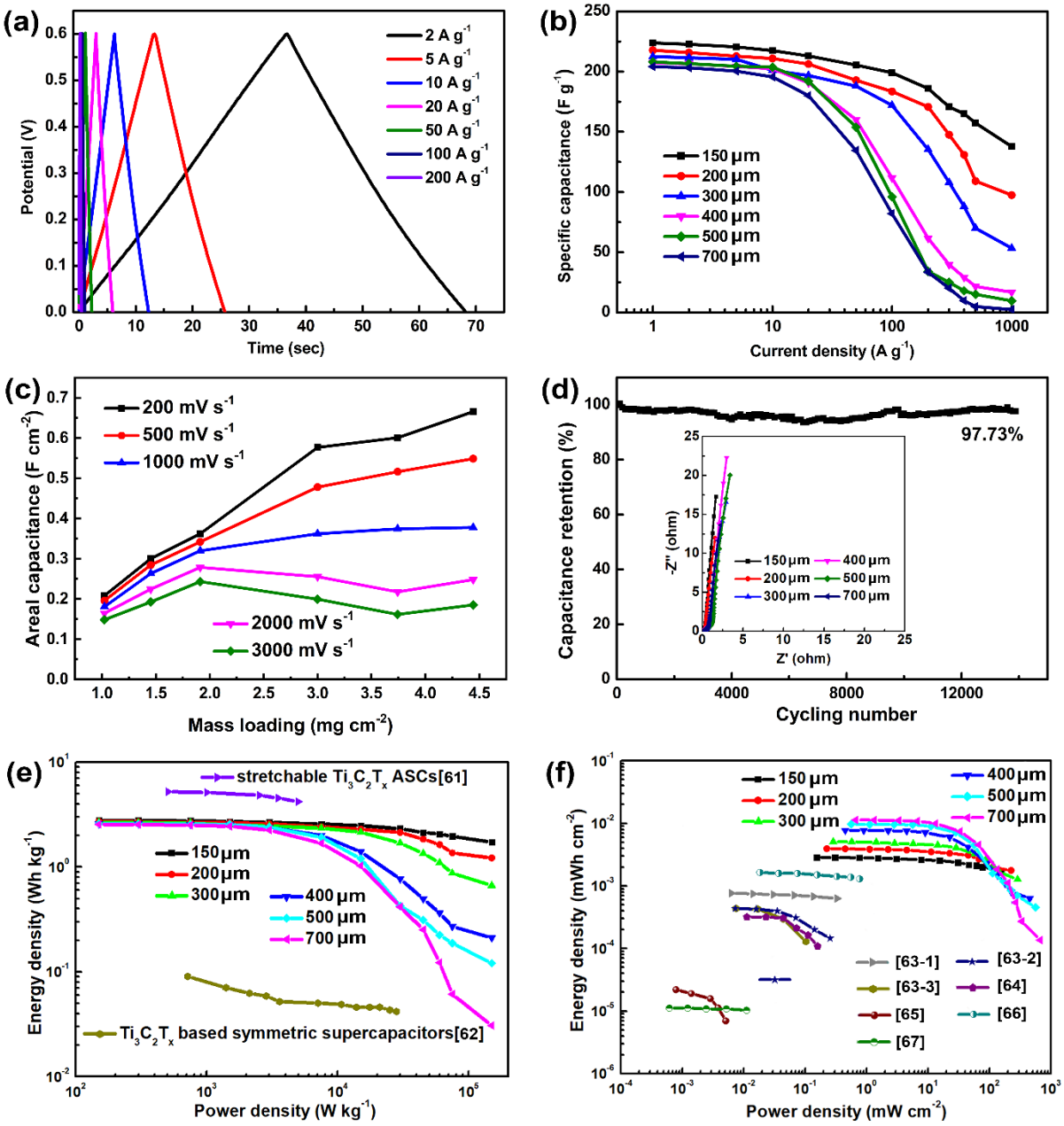

Figure 6. **Electrochemical performance of the vertically aligned $Ti_3C_2T_x$ films with thicknesses of 150, 200, 300, 400, 500 and 700 µm (produced from 70 mg mL^{-1} slurry). (a) Galvanostatic charge-discharge profiles of the 300 µm thickness $Ti_3C_2T_x$ film at 2, 5, 10, 20, 50, 100, 200 A g^{-1}. (b) Gravimetric rate performance of the vertically aligned $Ti_3C_2T_x$ films at current densities ranging from 1 to 1,000 A g^{-1}. (c) Areal capacitance as a function of the mass loading at scan rates from 200 to 3,000 mV s^{-1}. The**

mass loading points (from left to right) correspond to films of 150, 200, 300, 400, 500 and 700 µm thickness. (d) Cycling stability of a vertically aligned $Ti_3C_2T_x$ electrode (thickness of 300 µm) tested by galvanostatic cycling at a current density of 10 A g^{-1} showing over 97 % capacitance retention after 14,000 cycles. The inset shows Nyquist plots of electrochemical impedance spectroscopy (EIS) for different thicknesses of vertically aligned $Ti_3C_2T_x$ films, tested at 0 V. Ragone plots of the two-electrodes $Ti_3C_2T_x$ supercapacitor displaying the gravimetric (e) and areal (f) energy and power densities achieved by the vertically aligned $Ti_3C_2T_x$ films with the comparison to other MXene/graphene electrodes reported in the literature, [63-1: I-$Ti_3C_2T_x$] [63-2: Y-$Ti_3C_2T_x$] [63-3: Y-Ti_3CNT_x][63] [64: extrusion printed $Ti_3C_2T_x$ micro-supercapacitor][64] [65: spray-coated graphene][65] [66: screen printed $Ti_3C_2T_x$][66] [67: graphene/$Ti_3C_2T_x$ transparent electrode][67].

Galvanostatic charge-discharge (GCD) characteristics of the films at different current densities from 1 to 1,000 A g^{-1} were tested and the representative plots of 2, 5, 10, 20, 50, 100 and 200 A g^{-1} are exhibited in **Fig. 6a**. We can see linear symmetrical triangular charge-discharge lines with negligible IR drop, suggesting good energy storage behaviour and high electrical conductivity of the samples. The highest specific capacitance value of 224 F g^{-1} was achieved at a current density of 1 A g^{-1} for the 150 µm thick sample, originating from the effective utilization of the electrochemically active surface area. As the current density is further increased to an ultrahigh current density of 1,000 A g^{-1}, a high specific capacitance of 137.8 F g^{-1} can still be kept, which is much higher than the rate performances reported in most literature [61–67], showing the excellent rate performance achieved with the vertical microstructure of the electrode. The GCD rate performance of all samples were evaluated and displayed in **Fig. 6b**. The specific gravimetric capacitance value for the 150 µm sample is retained at 89 % and 62 % when the current density is increased from 1 to 100 A g^{-1} and 1 to 1,000 A g^{-1} respectively. Further, 81 % of the specific gravimetric capacitance (from 1 to 100 A g^{-1}) is retained when the thickness of the electrode increases to 300 µm. This is attributed to the porous lamellar structure facilitating the efficient mass transport of the electrolyte ions. **Fig. 6c** demonstrates the areal capacitance at varying scan rates as a function of mass loading

(the areal mass loading increase corresponds to the increase in thickness from 150 to 700 µm). At scan rates below 500 mV s^{-1}, the areal capacitance increases almost linearly with mass loading up to 4.5 mg cm^{-2}, indicating the importance of the electrode morphology on the electrochemical behaviour, i.e. the ease of electrolyte transport into the porous electrode and increase of the active surface area participating in the electrochemical response. By increasing the scan rate above 500 mV s^{-1}, the relationship between areal capacitance and mass loading gradually deviates from linearity as the mass of electrodes increases above 3 mg cm^{-2}. Above a scan rate of 1,000 mV s^{-1}, capacitive equilibration is achieved for mass loadings above 2 mg cm^{-2}.

With the aim of investigating the cycling stability of films, a long-term cycling retention test at a high current density of 10 A g^{-1} was carried out (**Fig. 6d**). After 14,000 continuous cycles, the 300 µm thick sample retained 97.7 % of the initial value (after 1,000 cycle pre-activation), indicating that the electrochemical behaviour is highly reversible. The inset of **Fig. 6d** depicts the electrochemical impedance spectroscopy (EIS) of samples of various thicknesses. The equivalent series resistance of the different electrodes is around 0.5 Ω, regardless of the electrode thickness, demonstrating a fast charge transportation. The plots of all different electrodes are almost vertical in the low frequency region, suggesting an excellent capacitive response in the vertically aligned $Ti_3C_2T_x$ films electrode. The Ragone plots in **Figs. 6e** and **6d** graphically depict the characteristics of the gravimetric, and areal energy and power densities of the corresponding supercapacitors based on the modified $Ti_3C_2T_x$ electrodes. The device made of 150 µm thick $Ti_3C_2T_x$ electrodes exhibits an energy density of 2.8 Wh kg^{-1} at a power density of 150 W kg^{-1}. Furthermore, when the power is increased by 1,000 times (150 kW kg^{-1}), the energy density is maintained at 62 % (1.7 Wh kg^{-1}). When the electrode thickness is increased to 200 and 300 µm, the energy densities can be maintained at 68 % and 51 %

respectively, of the initial value while the power density increases by a factor of 300 (to 45 kW kg^{-1}), reflecting the ultrahigh power density potential of these devices. The vertically aligned two-electrode supercapacitors developed in this work are able to achieve one of the highest recorded values of power density compared to other MXene or graphene related works (as seen in **Fig. 6f**). The 150 µm thick electrode at a high-power density of 154 mW cm^{-2}, shows an energy density of 1.8 µWh cm^{-2} without sacrificing the inherent advantage of supercapacitors. On the other hand, a high areal power density of 667 mW cm^{-2} can be achieved at 4,444 mA cm^{-2} for the 700 µm thick electrode. The superior electrochemical performance of these $Ti_3C_2T_x$ electrodes can be attributed to the intrinsically high electrical conductivity of the exfoliated $Ti_3C_2T_x$ flakes (2,963 and 4,279 S cm^{-1} for MXene films made for 45 and 70 mg mL^{-1} slurries respectively) and the vertically aligned architecture produced by the FaTC manufacturing method. The directional channels, which run parallel to the direction of ion transport are an important design factor, as they overcome rate limitations, in contrast to a restacking electrode film produced by conventional electrode casting processes.

Conclusion

A key challenge with 2D materials conventional electrode preparation methods is their microstructural restacking. In this work, vertically aligned MXene electrodes were prepared via a facile and scalable FaTC method, minimising restacking, and producing a favourable architecture for electrolyte impregnation and diffusion. This enabled the realization two-electrode (up to 300 µm thickness each) supercapacitors with nearly thickness independent electrochemical performance across a wide range of high scan rates and current densities. Furthermore, the industrially compatible $Ti_3C_2T_x$ films demonstrated remarkable gravimetric and areal power densities for 150 to 700 µm thicknesses. This was possible due to the

preparation of MXene slurries with shear thinning behaviour, yet sufficiently retained storage modulus to facilitate the tape casting process while allowing the formation of lamellar ice crystals that template the vertically aligned MXene architecture within films. This work demonstrates the viability of FaTC for potential large-scale fabrication of EES device electrodes with greater thickness without losing performance during fast charge-discharge cycling. Despite encouraging initial results, there are several challenges and opportunities for subsequent work, including optimization of freeze and tape casting parameters to allow for the enhancement of solid loading, choice of substrate, and additives to enhance the energy density in addition to the development of multi-materials fabrication protocols. The authors hope that the processing route showcased within this work highlights its potential for the development of 2D material assemblies in various electronic and composite applications.

Acknowledgements

This work was supported by the Henry Royce Institute for Advanced Materials, funded through EPSRC grants EP/R00661X/1, EP/S019367/1, EP/P025021/1 and EP/P025498/1. The authors would like to acknowledge the University of Manchester for the President's Doctoral Scholar Award. R.A.W.D. thanks EPSRC for funding through the grants EP/R023034/1 and EP/N032888/1. The authors also acknowledge the Henry Mosley X-ray Imaging Facility and the Department of Materials X-ray Diffraction Suite at the University of Manchester and the technical support, advice and assistance provided by Dr. John E. Warren. S.B. would like to thank Heilongjiang Huasheng Graphite Co. Ltd. for funding.

References

[1] Y. Gogotsi, P. Simon, *Science.* **2011**, *334*, 917.

[2] B. Anasori, M. R. Lukatskaya, Y. Gogotsi, *Nat. Rev. Mater.* **2017**, *2*, 16098.

[3] H. Tang, Q. Hu, M. Zheng, Y. Chi, X. Qin, H. Pang, Q. Xu, *Prog. Nat. Sci. Mater. Int.* **2018**, *28*, 133.

[4] M. R. Lukatskaya, S. M. Bak, X. Yu, X. Q. Yang, M. W. Barsoum, Y. Gogotsi, *Adv. Energy Mater.* **2015**, *5*, 1500589.

[5] C. J. Zhang, B. Anasori, A. Seral-Ascaso, S. H. Park, N. McEvoy, A. Shmeliov, G. S. Duesberg, J. N. Coleman, Y. Gogotsi, V. Nicolosi, *Adv. Mater.* **2017**, *29*, 1702678.

[6] S. Abdolhosseinzadeh, R. Schneider, A. Verma, J. Heier, F. Nüesch, C. (John) Zhang, *Adv. Mater.* **2020**, *32*, 2000716.

[7] M. Q. Zhao, C. E. Ren, Z. Ling, M. R. Lukatskaya, C. Zhang, K. L. Van Aken, M. W. Barsoum, Y.

Gogotsi, *Adv. Mater.* **2015**, *27*, 339.

[8] Z. Ling, C. E. Ren, M. Q. Zhao, J. Yang, J. M. Giammarco, J. Qiu, M. W. Barsoum, Y. Gogotsi, *Proc. Natl. Acad. Sci.* **2014**, *111*, 16676.

[9] H. An, T. Habib, S. Shah, H. Gao, M. Radovic, M. J. Green, J. L. Lutkenhaus, *Sci. Adv.* **2018**, *4*, eaaq0118.

[10] S. Korkut, J. D. Roy-Mayhew, D. M. Dabbs, D. L. Milius, I. A. Aksay, *ACS Nano* **2011**, *5*, 5214.

[11] T. Hu, M. Hu, Z. Li, H. Zhang, C. Zhang, J. Wang, X. Wang, *Phys. Chem. Chem. Phys.* **2016**, *18*, 20256.

[12] Y. Xia, T. S. Mathis, M. Q. Zhao, B. Anasori, A. Dang, Z. Zhou, H. Cho, Y. Gogotsi, S. Yang, *Nature* **2018**, *557*, 409.

[13] R. Tian, M. Breshears, D. V Horvath, J. N. Coleman, *ACS Nano* **2020**, *14*, 3129.

[14] M. R. Lukatskaya, B. Dunn, Y. Gogotsi, *Nat. Commun.* **2016**, *7*, 12647.

[15] J. Luo, C. Fang, C. Jin, H. Yuan, O. Sheng, R. Fang, W. Zhang, H. Huang, Y. Gan, Y. Xia, C. Liang, J. Zhang, W. Li, X. Tao, *J. Mater. Chem. A* **2018**, *6*, 7794.

[16] J. Luo, C. Wang, H. Wang, X. Hu, E. Matios, X. Lu, W. Zhang, X. Tao, W. Li, *Adv. Funct. Mater.* **2019**, *29*, 1805946.

[17] J. Luo, W. Zhang, H. Yuan, C. Jin, L. Zhang, H. Huang, C. Liang, Y. Xia, J. Zhang, Y. Gan, X. Tao, *ACS Nano* **2017**, *11*, 2459.

[18] M. R. Lukatskaya, O. Mashtalir, C. E. Ren, Y. Dall'Agnese, P. Rozier, P. L. Taberna, M. Naguib, P. Simon, M. W. Barsoum, Y. Gogotsi, *Science (80-.).* **2013**, *341*, 1502.

[19] Y. Xu, Z. Lin, X. Zhong, X. Huang, N. O. Weiss, Y. Huang, X. Duan, *Nat. Commun.* **2014**, *5*, 1.

[20] Z. Fan, Y. Wang, Z. Xie, D. Wang, Y. Yuan, H. Kang, B. Su, Z. Cheng, Y. Liu, *Adv. Sci.* **2018**, *5*,

1800750.

[21] J. Yang, H. Wu, M. Zhu, W. Ren, Y. Lin, H. Chen, F. Pan, *Nano Energy* **2017**, *33*, 453.

[22] M. R. Lukatskaya, S. Kota, Z. Lin, M. Q. Zhao, N. Shpigel, M. D. Levi, J. Halim, P. L. Taberna, M. W. Barsoum, P. Simon, Y. Gogotsi, *Nat. Energy* **2017**, *2*, 17105.

[23] V. Bayram, M. Ghidiu, J. J. Byun, S. D. Rawson, P. Yang, S. A. McDonald, M. Lindley, S. Fairclough, S. J. Haigh, P. J. Withers, M. W. Barsoum, I. A. Kinloch, S. Barg, *ACS Appl. Energy Mater.* **2020**, *3*, 411.

[24] W. Yang, J. Yang, J. J. Byun, F. P. Moissinac, J. Xu, S. J. Haigh, M. Domingos, M. A. Bissett, R. A. W. Dryfe, S. Barg, *Adv. Mater.* **2019**, *31*, 1902725.

[25] G. Tontini, M. Greaves, S. Ghosh, V. Bayram, S. Barg, *J. Phys. Mater.* **2020**, *3*, 022001.

[26] Y. Yoon, K. Lee, S. Kwon, S. Seo, H. Yoo, S. Kim, Y. Shin, Y. Park, D. Kim, J. Y. Choi, H. Lee, *ACS Nano* **2014**, *8*, 4580.

[27] Z. Bo, W. Zhu, W. Ma, Z. Wen, X. Shuai, J. Chen, J. Yan, Z. Wang, K. Cen, X. Feng, *Adv. Mater.* **2013**, *25*, 5799.

[28] S. Deville, E. Maire, A. Lasalle, A. Bogner, C. Gauthier, J. Leloup, C. Guizard, *J. Am. Ceram. Soc.* **2009**, *92*, 2489.

[29] S. Deville, E. Saiz, A. P. Tomsia, *Acta Mater.* **2007**, *55*, 1965.

[30] N. H. Fletcher, *Philos. Mag.* **1968**, *18*, 1287.

[31] P. Zhang, Q. Zhu, R. A. Soomro, S. He, N. Sun, N. Qiao, B. Xu, *Adv. Funct. Mater.* **2020**, 2000922.

[32] P. Zhang, R. A. Soomro, Z. Guan, N. Sun, B. Xu, *Energy Storage Mater.* **2020**, *29*, 163.

[33] Y. Chen, J. Bunch, T. Li, Z. Mao, F. Chen, *J. Power Sources* **2012**, *213*, 93.

[34] T. Liu, Y. Chen, S. Fang, L. Lei, Y. Wang, C. Ren, F. Chen, *J. Memb. Sci.* **2016**, *520*, 354.

[35] E. P. Gorzkowski, M. J. Pan, B. A. Bender, in *2011 Int. Symp. Appl. Ferroelectr. 2011 Int. Symp. Piezoresponse Force Microsc. Nanoscale Phenom. Polar Mater. ISAF/PFM 2011*, **2011**.

[36] K. Araki, J. W. Halloran, *J. Am. Ceram. Soc.* **2005**, *88*, 1108.

[37] L. Ren, Y. P. Zeng, D. Jiang, *J. Am. Ceram. Soc.* **2007**, *90*, 3001.

[38] L. M. Wang, Z. F. Tang, J. Lin, X. D. He, C. S. Chen, C. H. Chen, *J. Mater. Chem. A* **2019**, *7*, 17376.

[39] A. Daraghmeh, S. Hussain, L. Servera, E. Xuriguera, M. Blanes, F. Ramos, A. Cornet, A. Cirera, *Mater. Res. Express* **2017**, *4*, 025007.

[40] R. A. Susantyoko, F. Parveen, I. Mustafa, S. Almheiri, *Ionics.* **2019**, *25*, 265.

[41] Y. Hwa, E. Yi, H. Shen, Y. Sung, J. Kou, K. Chen, D. Y. Parkinson, M. M. Doeff, E. J. Cairns, *Nano Lett.* **2019**, *19*, 4731.

[42] X. Sang, Y. Xie, M. W. Lin, M. Alhabeb, K. L. Van Aken, Y. Gogotsi, P. R. C. Kent, K. Xiao, R. R. Unocic, *ACS Nano* **2016**, *10*, 9193.

[43] M. Alhabeb, K. Maleski, B. Anasori, P. Lelyukh, L. Clark, S. Sin, Y. Gogotsi, *Chem. Mater.* **2017**, *29*, 7633.

[44] L. Verger, C. Xu, V. Natu, H. M. Cheng, W. Ren, M. W. Barsoum, *Curr. Opin. Solid State Mater. Sci.* **2019**, *23*, 149.

[45] E. Wu, J. Wang, H. Zhang, Y. Zhou, K. Sun, Y. Xue, *Mater. Lett.* **2005**, *59*, 2715.

[46] Swanson, Howard E, *United States Department Of Commerce National Bureau Of Standards* **1967**, *Circular 539 Vol 3*.

[47] J. Lewis, D. Schwarzenbach, H. D. Flack, *Acta Crystallogr. Sect. A* **1982**, *38*, 733.

[48] M. Y. Tashmetov, V. T. Em, C. H. Lee, H. S. Shim, Y. N. Choi, J. S. Lee, *Phys. B Condens. Matter* **2002**, *311*, 318.

[49] B. Bitterlich, C. Lutz, A. Roosen, *Ceram. Int.* **2002**, *28*, 675.

[50] M. Jabbari, R. Bulatova, A. I. Y. Tok, C. R. H. Bahl, E. Mitsoulis, J. H. Hattel, *Mater. Sci. Eng. B Solid-State Mater. Adv. Technol.* **2016**, *212*, 39.

[51] A. M. Anderson, M. G. Worster, *Langmuir* **2012**, *28*, 16512.

[52] A. M. Anderson, M. G. Worster, *J. Fluid Mech.* **2014**, *758*, 786.

[53] T. Waschkies, R. Oberacker, M. J. Hoffmann, *Acta Mater.* **2011**, *59*, 5135.

[54] S. Deville, E. Maire, G. Bernard-Granger, A. Lasalle, A. Bogner, C. Gauthier, J. Leloup, C. Guizard, *Nat. Mater.* **2009**, *8*, 966.

[55] W. W. Mullins, R. F. Sekerka, *J. Appl. Phys.* **1964**, *35*, 444.

[56] S. Deville, E. Maire, A. Lasalle, A. Bogner, C. Gauthier, J. Leloup, C. Guizard, *J. Am. Ceram. Soc.* **2009**, *92*, 2497.

[57] H. Bai, Y. Chen, B. Delattre, A. P. Tomsia, R. O. Ritchie, *Sci. Adv.* **2015**, *1*, e1500849.

[58] S. K. Kim, H. J. Kim, J. C. Lee, P. V. Braun, H. S. Park, *ACS Nano* **2015**, *9*, 8569.

[59] J. Yun, D. Kim, G. Lee, J. S. Ha, *Carbon N. Y.* **2014**, *79*, 156.

[60] M. Acerce, D. Voiry, M. Chhowalla, *Nat. Nanotechnol.* **2015**, *10*, 313.

[61] T. H. Chang, T. Zhang, H. Yang, K. Li, Y. Tian, J. Y. Lee, P. Y. Chen, *ACS Nano* **2018**, *12*, 8048.

[62] R. B. Rakhi, B. Ahmed, M. N. Hedhili, D. H. Anjum, H. N. Alshareef, *Chem. Mater.* **2015**, *27*, 5314.

[63] C. J. Zhang, M. P. Kremer, A. Seral-Ascaso, S. H. Park, N. McEvoy, B. Anasori, Y. Gogotsi, V. Nicolosi, *Adv. Funct. Mater.* **2018**, *28*, 1705506.

[64] C. (John) Zhang, L. McKeon, M. P. Kremer, S. H. Park, O. Ronan, A. Seral-Ascaso, S. Barwich, C. Coileáin, N. McEvoy, H. C. Nerl, B. Anasori, J. N. Coleman, Y. Gogotsi, V. Nicolosi, *Nat. Commun.* **2019**, *10*, 1.

[65] H. Li, Y. Hou, F. Wang, M. R. Lohe, X. Zhuang, L. Niu, X. Feng, *Adv. Energy Mater.* **2017**, *7*, 1601847.

[66] C. (John) Zhang, V. Nicolosi, *Energy Storage Mater.* **2019**, *16*, 102.

[67] C. J. Zhang, B. Anasori, A. Seral-Ascaso, S. H. Park, N. McEvoy, A. Shmeliov, G. S. Duesberg, J. N. Coleman, Y. Gogotsi, V. Nicolosi, *Adv. Mater.* **2017**, *29*, 1702678.